The influence of hydrogen permeation on the protection performance of the Cu coating of nuclear waste containers

Xiangju Liu [a,b], Nazhen Liu [a,b,c,*], James J. Noël [c], David W. Shoesmith [c], Jian Chen [c], Baorong Hou [a,b]

[a] Key Laboratory of Marine Environmental Corrosion and Bio-fouling, Institute of Oceanology, Chinese Academy of Sciences, Qingdao 266071, China
[b] Open Studio for Marine Corrosion and Protection, Pilot National Laboratory for Marine Science and Technology (Qingdao), Qingdao 266237, China
[c] Chemistry Department, Western University, London, Ontario N6A 5B7, Canada

ARTICLE INFO

ABSTRACT

Hydrogen permeation and corrosion behaviour of Cu-coated carbon steel under simulated nuclear waste disposal conditions of the Beishan area have been investigated. The permeation current (with -500 $\mu A \cdot cm^{-2}$ charging current) decreased from 3778 to 141 and 47 $nA.cm^{-2}$ respectively when 5 and 10 μm thick Cu coatings were electrodeposited on the steel. The XRD analysis suggests the formation of CuH during the hydrogen charging treatment, and its subsequent decomposition formed a protective $CuOH/Cu_2O$ layer on the charging surface when exposed to simulated groundwater for 44 h. No damage to the Cu coating-steel interface was observed in the cross-section analysis.

1. Introduction

The concept of deep geological repositories (DGR) for the permanent disposal of high-level nuclear waste is under investigation in many countries. The repository concept is based on multiple barriers, normally including the waste form, durable metal containers, a clay buffer and seals around the container, and a deep geologic environment [1–3]. A key barrier in this sequence is the corrosion-resistant container, designed to isolate the waste from the repository environment [4,5]. Carbon steel, due to its strength and low cost, is a candidate material for the structural element of the container [6,7]. In many countries, the application of a Cu coating to provide enhanced container lifetimes is under consideration, since Cu is anticipated to have a very low corrosion rate under repository conditions [5,8].

Cu corrosion under repository conditions has been extensively studied in short-term [9,10] and long-term [11–14] electrochemical experiments, by weight loss measurements, and by measuring hydrogen generation [15], in solutions, and in bentonite [16,17]. However, there are few studies concerning the influence of hydrogen permeation on the integrity and corrosion performance of Cu coatings [18]. If defects are present in the Cu coating, exposure of the steel vessel under the anticipated anoxic conditions in a DGR could produce H_2, introducing the possibility of delamination of the coating [19–21].

In a DGR, diffusible hydrogen atoms could be produced mainly by two possible routes: (1) Water radiolysis by γ radiation, which can penetrate the container and reach the interface between the container surface and the corrosive media; (2) Proton reduction, which will be the primary cathodic reaction on steel under anoxic repository conditions. The hydrogen atoms formed on the container surface will lead to either H_2 evolution or absorption and diffusion into the metal. Absorbed hydrogen atoms would be trapped at material defects (e.g., microcracks, inclusions), resulting in materials degradation [22–27].

Hydrogen permeation through a metallic membrane using a Devanathan-Stachurski double cell (DS cell) [28] is widely used to study hydrogen diffusivity in different materials. On the hydrogen entry surface of the metallic membrane, the production of hydrogen atoms can be controlled galvanostatically, potentiostatically, or under free corrosion conditions. A fraction of the hydrogen atoms produced are then absorbed by the metal, diffuse through the metallic membrane, and are finally desorbed at the exit surface, where a constant potential is applied to ensure that all hydrogen atoms which penetrate the steel are oxidized, with the current being a measure of the hydrogen permeation flux.

In this work, experiments on hydrogen permeation through a carbon steel membrane electroplated with Cu are conducted in simulated

---

groundwater of the Beishan area (the preselected repository site for high-level nuclear waste in China) to study the influence of the copper coating on hydrogen permeation. The influence of hydrogen permeation on the protection performance of copper coatings is also analyzed electrochemically before and after hydrogen charging.

2. Materials and experimental

2.1. Materials and specimens

Commercially available Q235 carbon steel membranes with a chemical composition in wt% of 0.14% C, 0.1% Si, 0.41% Mn, 0.015% P and 0.038% S, a diameter of 42 mm, and a thickness of 1 mm were provided by Shengxin Technology Co., Ltd. (Shandong, China). Prior to Cu electroplating, both sides of the membranes were abraded with a series of grit papers (120#, 400#, 600#, 800#, 1000# and 1500#). The average thickness of different polished membranes was 0.75 mm ± 0.30 mm. The thickness of each membrane was uniform. The polished membranes were then washed with deionized water (resistivity = 18.2 MΩ·cm, Smart-N ultrapure water system, Heal Force Bio-Meditech Holdings Ltd., China), ultrasonically cleaned using ethanol (reagent grade), and dried using cold ultra-pure N_2 gas (99.999%). Copper sheets (T2) with a chemical composition in wt% of 0.005% Zn, 0.005% Pb, 0.002% Sn, 0.005% Ni, 0.005% Fe, 0.002% Sb, 0.005% S, 0.002% As, 0.001% Bi were provided by Shengxin Technology Co., Ltd. (Shandong, China).

2.2. The fabrication of Cu-coated carbon steel specimens

The schematic of the Cu-coated carbon steel specimen is shown in Fig. 1a. To increase the adhesion between the Cu coating and the carbon steel substrate, a thin nickel interlayer (~600 nm) was first plated onto the Q235 substrate. Before the plating of the Ni interlayer, the surface of the Q235 specimen was activated for several seconds in a 0.1 mol·L^{-1} HCl solution and washed with deionized water. A 99.5 wt% Ni plate was used as the plating anode. A current density of 10 mA·cm^{-2} was applied for 3 min, and the Ni-plated specimen then washed with deionized water. The thickness of the nickel coating was about 600 nm. In the subsequent copper-plating, a 70 × 60 × 3 mm^3 phosphor copper (0.05–0.1 wt% of P) plate was employed as the plating anode, and a copper-plating current density of 10 mA·cm^{-2} was applied for 60 min. The Cu coating was then polished to a thickness of either 5 or 10 μm using 1000# and 1500# grit papers. The compositions of electrolytes used for plating the Ni interlayer and Cu coating are listed in Table 1.

The other side of the Q235 substrate (facing the hydrogen detection cell where a constant potential was applied and the permeated hydrogen atoms were oxidized) was electroplated with a thin nickel layer (indicated as Ni* in Fig. 1a) in a Watt's bath (NiSO$_4$·6 H$_2$O 250 g·L^{-1},

Table 1
Composition of plating solutions utilized in this work.

Solution	Component	Concentration (g·L^{-1})
Nickel-plating	NiSO$_4$·6 H$_2$O	120
	NaCl	8
	H$_3$BO$_3$	35
	Na$_2$SO$_4$·10 H$_2$O	30
	Sodium dodecyl sulfate (SDS)	0.06
Copper-plating	CuSO$_4$·5 H$_2$O	220
	H$_2$SO$_4$	64
	HCl	0.03
	Polyethylene glycol (PEG, molecular weight 6000)	0.2
	Sodium 3,3′-dithiodipropane sulfonate (SPS)	8.0×10^{-3}
	2-Imidazolidinetone (N)	2.0×10^{-4}

NiCl$_2$·6 H$_2$O 45 g·L^{-1}, H$_3$BO$_3$ 40 g·L^{-1}) at room temperature with a current density of 3 mA·cm^{-2} for 3 min [29]. The thickness of the Ni* coating was about 180 nm.

2.3. Simulated groundwater composition

The typical composition of groundwater at Beishan is shown in Table 2 [30]. In Section 3.1, the electrolyte was prepared according to Table 2. Since hydrogen charging produces hydroxide ions and alkaline conditions near the Cu coating surface, HCO$_3^-$, Ca^{2+} and Mg^{2+} ions in groundwater form calcareous deposits on the Cu coating [31–35], resulting in errors in the analysis of coating performance before and after hydrogen charging. Thus, in Sections 3.2–3.7, only Cl$^-$ and SO$_4^{2-}$ anions were used to prepare the groundwater, with Na$^+$ cations to ensure charge balance, as listed in Table 3.

2.4. Hydrogen permeation experiments

A modified DS cell was used for the hydrogen permeation tests, Fig. 1b. The fabricated working electrode (indicated as W in Fig. 1b) with an exposure area of 3.53 cm^2 on both sides was mounted between Cell 1 and Cell 2–1. The side facing Cell 1 (the hydrogen detection cell) was coated with the Ni* layer to prevent steel oxidation and promote the ionization reaction of hydrogen [36]. Cell 1 was filled with 0.2 mol·L^{-1} NaOH solution and polarized potentiostatically at 0.05 V vs. a HgO/Hg/1.0 mol·L^{-1} KOH reference electrode (R1) (0.098 V vs. NHE), using a Model PS-8 Multichannel Potentiostat/Galvanostat (TOHO Technical Research Co., Ltd. Japan). The polarization lasted for at least 24 h to ensure that the background anodic current was less than 0.1 μA·cm^{-2}. Then, the simulated groundwater was added to Cell 2 (the hydrogen charging cell, including Cell 2–1 and 2–2). A standard

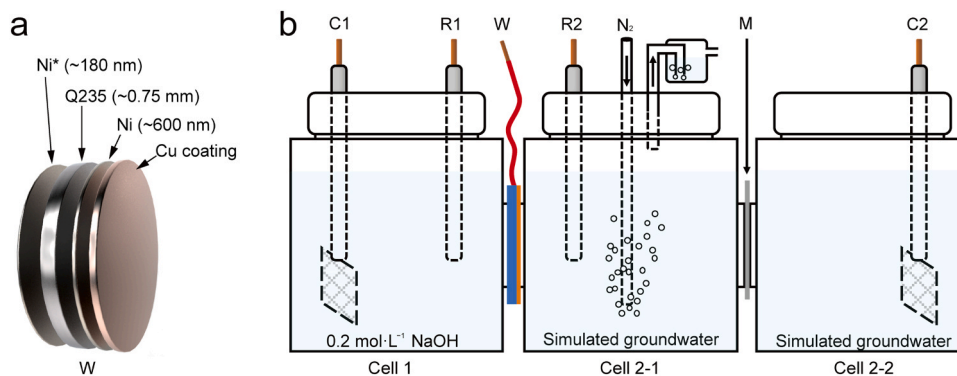**Fig. 1.** Schematics of the Cu-coated carbon steel specimen (a) and the modified Devanathan-Stachurski electrochemical cells (b). C1, counter electrode of hydrogen detection side; R1, reference electrode of hydrogen detection side (Hg/HgO/1.0 mol·L^{-1} KOH); W, working electrode; R2, reference electrode of hydrogen entry side (SCE); M, proton exchange membrane; C2, counter electrode of hydrogen entry side.

Table 2
Typical chemical composition of groundwater at Beishan area of China.

Ion species	Na⁺	K⁺	Ca²⁺	Mg²⁺	HCO₃	Cl⁻	SO₄²⁻	NO₃⁻
Concentration (mg·L⁻¹)	1170.07	20.00	219.43	57.37	96.37	1261.33	1259.67	27.10

Table 3
Composition of simulated groundwater in this work.

Component	NaCl	Na₂SO₄
Concentration (mg·L⁻¹)	2079.3	1860.7
Specifications (Purity)	≥ 99.999% (metals basis)	≥ 99.999% (metals basis)
Brand	Aladdin	Aladdin

three-electrode cell with a Pt plate counter electrode (C2) and a saturated calomel reference electrode (SCE) (R2) was used. The counter electrode compartment (Cell 2–2) was separated from Cell 2–1 by a proton exchange membrane (Nafion 117) to avoid any possible influence of the anodic reaction products at the counter electrode on the hydrogen entry [32,37]. For Cell 2–1, continuous sparging with ultra-pure N_2 was maintained during the experiments. Prior to hydrogen charging, electrodes were cathodically cleaned at − 1.6 V vs. SCE for 2 min and then at − 1.15 V vs. SCE for 2 min. The hydrogen charging current density was − 500 μA·cm⁻².

2.5. Electrochemical experiments

Electrochemical tests were performed before and after electrochemical hydrogen charging using the Ivium pocketSTAT2 (Ivium Technologies B.V., Netherlands). Prior to each test, the open circuit potential (OCP) was allowed to achieve a steady state (e.g., the potential change within 60 s was less than 1 mV). Electrochemical impedance spectroscopy (EIS) was performed with a sinusoidal potential perturbation of ± 10 mV vs. OCP. The corresponding current response was measured over a frequency range from 10^5 Hz to 10^{-3} Hz, with 10 data points recorded per decade. EIS data were fitted using Zview software.

2.6. Surface analysis

The XRD analysis used to determine the composition of calcareous deposits was performed on a Rigaku Ultime IV X-ray diffractometer (Rigaku Co., Japan), with the 2θ angle scanned from 10° to 80° at a rate of 5°/min.

For the XRD analysis of the hydrogen-charged surface, copper sheets (1 ×1 ×0.2 cm³) and copper coating (stripped from the carbon steel substrate), after being hydrogen charged, were removed immediately from the cell, washed with deionized water for 1 min, dehydrated with ethanol, dried with cold ultra-pure N_2 gas, and stored under vacuum (P_e = ~0.088 MPa). The X-ray diffraction measurements were performed using a PANalytical diffractometer (Malvern Panalytical Ltd., UK) with a Cu Kα target under an Ar atmosphere at − 50 °C, and the 2θ angle was scanned from 30° to 80° at a rate of 1°/min.

After hydrogen charging and the subsequent electrochemical tests, the specimens were first disassembled from the cell, rinsed with deionized water and ethanol (99.8%, reagent grade), and dried with cold ultra-pure N_2 gas. For the cross-section samples, the specimens were cut using a saw and sealed in epoxy resin. Then the cross-sections were abraded with a series of grit papers (800#, 1000#, 1500#, 2000# and 3000#), ultrasonically cleaned using ethanol (reagent grade) for 1 min, and dried using cold ultra-pure N_2. All samples were packaged under vacuum (P_e = ~0.088 MPa) using a commercial vacuum packaging machine until surface analysis could be performed. The surface and cross-sectional morphologies of specimens were observed using a scanning electron microscope (SEM, Hitachi Regulus8100, Hitachi Ltd., Japan) and an FEI Scios 2 HiVac focused ion beam (FIB-SEM, Thermo

Fisher Scientific Inc., USA). The chemical composition of the surfaces was analyzed qualitatively by energy-dispersive X-ray spectroscopy (EDX, IXRF-SDD3330-A5501, IXRF Systems Inc., USA). X-ray photoelectron spectroscopy (XPS) measurements were performed on a Thermo ESCALAB 250Xi (Thermo Fisher Scientific Inc., USA) with an Al Kα X-ray as the incident beam and the C 1 s peak at 284.8 eV as the internal standard. In the XPS depth profiling measurement, the surface was etched at a rate of 1 nm/s. The XPS spectra were fitted using Avantage software. The Cu $L_3M_{4,5}M_{4,5}$ (LMM) spectra were fitted using standard spectra for Cu_2O and Cu (provided by Avantage) based on a nonlinear least squares method.

3. Results and discussion

3.1. The retarding effect of a Cu coating on hydrogen permeation

As mentioned in Section 2.2, a thin nickel interlayer (~600 nm) was first plated onto the Q235 substrate to increase the adhesion between the Cu coating and the carbon steel substrate. Fig. 2 shows the hydrogen permeation current density (i_p)-time curves of Q235, Q235 with a ~600 nm Ni coating (Q235 +Ni) and Q235 +Ni with 5 μm and 10 μm Cu coatings under the hydrogen charging current of − 500 μA·cm⁻². The background current density of i_p has been removed, but a current of 1 nA·cm⁻² is retained in order to plot the data in logarithmic coordinates. Fig. 2 shows that, for Q235 and Q235 +Ni, i_p increases rapidly as the hydrogen charging begins, and reaches the steady-state hydrogen permeation current density (i^∞, average value within 24 h before the end of the i_p-time curve) within approximately 3 days. The i^∞ of Q235 +Ni is only slightly lower than that of Q235, indicating that the thin Ni coating exerts little influence on hydrogen penetration into the underlying Q235. For Q235 +Ni with a Cu coating, there is an apparent increase in the time required to achieve the steady-state hydrogen permeation current, and a significant decrease in i^∞. Fig. 2 shows that a 5 μm Cu coating decreases i^∞ from 3167 nA·cm⁻² to 141 nA·cm⁻², and a further increase in coating thickness to 10 μm leads to the lowest i^∞ of 47 nA·cm⁻². The results in Fig. 2 demonstrate that hydrogen permeation through carbon steel can be inhibited significantly by a thin Cu coating
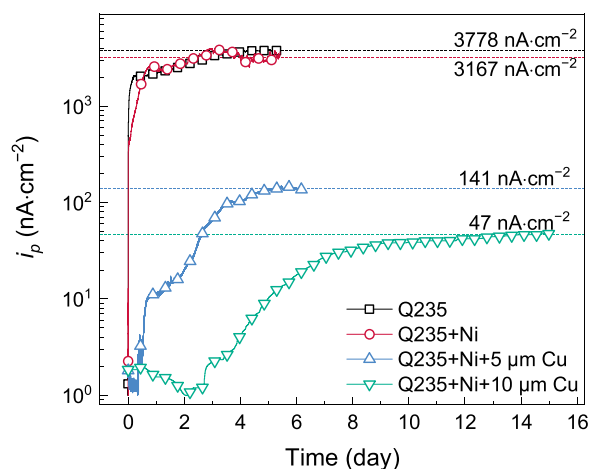

Fig. 2. The hydrogen permeation current density (i_p)-time curves recorded on Q235 and Q235 with Ni coatings and Q235 +Ni with 5 μm and 10 μm Cu coatings at a charging current of − 500 μA·cm⁻² in simulated groundwater (prepared according to Table 2).

of a few micrometers.

In neutral simulated groundwater (pH = 7.5), the hydrogen evolution reactions under electrochemical hydrogen charging conditions can be specified as follows [38]:

Volmer reaction (neutral or alkaline solution).

$$H_2O + M + e^- \rightarrow MH_{ads} + OH^- \tag{1}$$

Heyrovsky reaction (neutral or alkaline solution).

$$MH_{ads} + H_2O + e^- \rightarrow M + H_2 + OH^- \tag{2}$$

Tafel reaction.

$$2MH_{ads} \rightarrow 2\,M + H_2 \tag{3}$$

$$MH_{ads} \rightarrow MH_{abs} \tag{4}$$

where M represent the metal surface; MH_{ads} is the hydrogen adsorbed on the metal surface; and MH_{abs} is the hydrogen dissolved in the metal. During the electrochemical hydrogen charging process, H_2O will be reduced to adsorbed H atoms (MH_{ads}) (reaction 1). Some adsorbed hydrogen will form H_2 and then desorb from the surface (reactions 2 and 3). Some MH_{ads} will be absorbed (MH_{abs}) (reaction 4) and permeate into the metal.

Meanwhile, the hydroxide ion by-product of reaction 1 and 2 will cause a pH increase near the charging surface. Under these alkaline conditions, the HCO_3^-, Ca^{2+} and Mg^{2+} ions in simulated groundwater can form calcareous deposits such as $CaCO_3$ and $Mg(OH)_2$ on the charging surface (reactions 5–7) [32,39].

$$OH^- + HCO_3^- \rightarrow H_2O + CO_3^{2-} \tag{5}$$

$$CO_3^{2-} + Ca^{2+} \rightarrow CaCO_3\downarrow \tag{6}$$

$$Mg^{2+} + 2OH^- \rightarrow Mg(OH)_2\downarrow \tag{7}$$

The XRD results and optical images (inset) in Fig. 3 show that, after hydrogen charging, the surfaces were covered with a layer of deposits composed of $CaCO_3$ and $Mg(OH)_2$. The formation of calcareous deposits would induce errors in the calculation of the diffusion coefficient of hydrogen through the specimens, as discussed below.

The effective diffusion coefficients (D_{eff}) of hydrogen through the specimens were calculated using the standard methods specified in ASTM G148–97. Equations for modeling the hydrogen permeation curves using the breakthrough time, time lag, and Fourier and Laplace solutions of Fick's second law [26,40–44] are as follows;
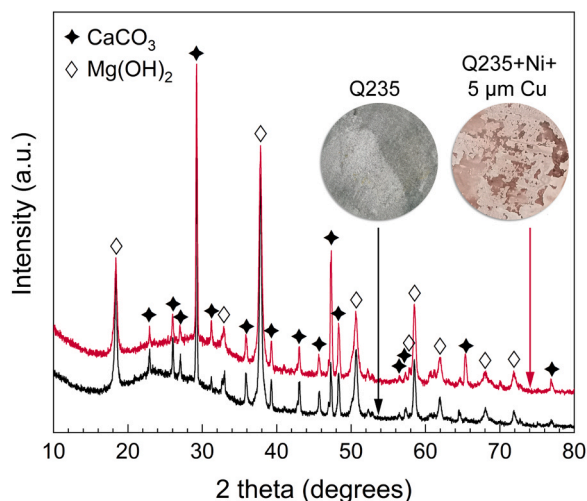
(a) Breakthrough time method [43],

$$t_b = L^2/15.3D_{eff} \tag{8}$$

(b) Time lag method [43],

$$t_{lag} = L^2/6D_{eff} \tag{9}$$

(c) Fourier solution for Fick's second law [41,44],

$$\frac{i_t}{i^\infty} = 1 + 2\sum_{n=1}^{\infty}(-1)^n\exp\left[-\frac{n^2\pi^2 D_{eff}t}{L^2}\right] \tag{10}$$

(d) Laplace solution for Fick's second law [41,44],

$$\frac{i_t}{i^\infty} = \frac{2L}{\sqrt{\pi D_{eff}t}}\sum_{n=0}^{\infty}\exp\left[-\frac{(2n+1)^2L^2}{4D_{eff}t}\right] \tag{11}$$

Fick's second law (Eq. 12) predicts how diffusion causes the concentration to change with respect to time. The Laplace & Fourier solutions are analytical tools based on the model which assumes the permeation rate is simply dependent on [H] gradients.

$$\frac{\partial C}{\partial t} = D\frac{\partial^2 C}{\partial x^2} \tag{12}$$

In these calculations, a thin membrane is regarded as the boundary condition, with a constant hydrogen concentration at the charging surface established by the applied current. In these equations, t_b is the breakthrough time obtained from the intersection of a tangential line on the linear section of the normalized permeation curve (Fig. 4) with the horizontal time axis; L the thickness of the specimen; D_{eff} the effective diffusion coefficient; t_{lag} the time lag, corresponding to the time when $i_t/i^\infty = 0.63$; i_t and i^∞ the currents measured in the hydrogen detection cell at time t and at steady-state, respectively. Ten terms (n = 10) of Eqs. (10 and 11) are considered to fit the experimental results using the least squares deviation method.

The D_{eff}s calculated using these methods are listed in Table 4. For Q235, there is a noticeable difference between the value calculated by the breakthrough time method and the other 3 methods. The D_{eff} value calculated from the breakthrough time was ~4 times higher than those derived from the other 3 methods. This difference could be caused by the formation of calcareous deposits, which have been reported to inhibit hydrogen permeation [45,46], and the thickening of these deposits with time. Due to the short t_b for carbon steel (306 s), the surface of the

Fig. 3. X-ray diffraction results of the calcareous deposits formed on the hydrogen charging surface in simulated groundwater (prepared according to Table 2).
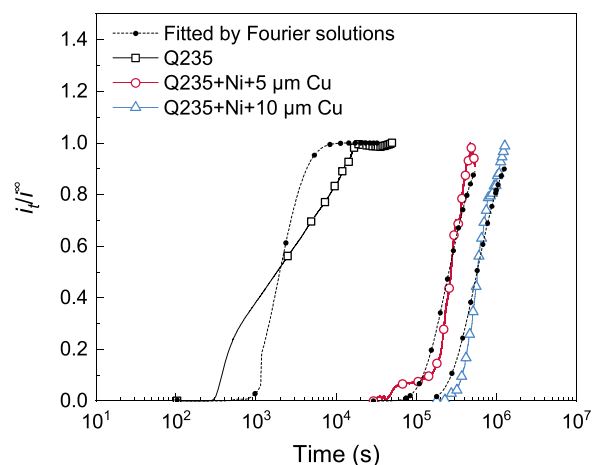

Fig. 4. Normalized hydrogen permeation curves for specimens of Q235 and Q235 +Ni with 5 μm and 10 μm Cu coatings under the charging current of − 500 μA·cm^{-2}.

Table 4

Hydrogen permeation data of Cu-coated Q235 carbon steel with different coating thickness.

Specimens	Q235	Q235 +Ni+Cu	Q235 +Ni+Cu
Thickness of Cu coating (μm)	—	5	10
Thickness of specimens, L (cm)	0.079	0.072	0.078
Breakthrough time, t_b (s)	306	156906	329329
Lag time, t_{lag} (s)	3567	293005	653488
Effective diffusion coefficient using various methods, D_{eff} (cm^2·s^{-1})			
Breakthrough method	1.3×10^{-6}	2.2×10^{-9}	1.2×10^{-9}
Lag time method	2.9×10^{-7}	3.0×10^{-9}	1.6×10^{-9}
Fourier solutions	3.0×10^{-7}	2.8×10^{-9}	1.5×10^{-9}
Laplace solutions	3.0×10^{-7}	2.8×10^{-9}	1.5×10^{-9}
Average of the last three methods	3.0×10^{-7}	2.9×10^{-9}	1.5×10^{-9}

carbon steel was not yet covered with a thick layer of calcareous deposits, leading to a large calculated D_{eff} using the breakthrough method. As the calcareous deposits thicken as the hydrogen charging process continues, their influence on the calculation of D_{eff} is observed. As a result, for Q235 +Ni+Cu specimens, t_b increases substantially; the calculated D_{eff}s using the breakthrough time are consistent with the other 3 methods. Table 4 shows that the calculated D_{eff} value of the 5 μm Cu-coated Q235 specimen is two orders of magnitude lower than that of pure Q235, and decreases while the Cu thickness increases. The calculated D_{eff} for Q235 coated with 10 μm Cu (1.5×10^{-9} cm^2·s^{-1}) is similar to the reported D for pure copper (1.8×10^{-9} cm^2·s^{-1}, 25 °C [47]). This similarity indicates that the full retarding effect of the Cu-coating on hydrogen permeation into the steel nuclear waste container has been achieved at 10 μm thickness.

The normalized hydrogen permeation curves and the curves fitted by the Fourier solution (Eq. 10) for Q235 and Q235 with either a 5 or 10 μm Cu coating are shown in Fig. 4. The observed inconsistency of the experimental and fitted curves suggests that the permeation of hydrogen through the specimen was not completely controlled by the diffusion of hydrogen [40]. The permeation transient for Q235 is less steep than that predicted by Fick's second law, which is probably caused by the continuous formation of calcareous deposits. The permeation transients for the Cu-coated Q235 specimens are slightly steeper than predicted by Fick's second law, indicating an apparent increase in trap occupancy of in Cu-coated steel.

3.2. The formation of CuH during hydrogen charging

As mentioned in Section 3.1, the formation of calcareous deposits on the charging surface (reactions 5–7) induces errors in the calculation of diffusion coefficients. It would also complicate the analysis of species formation and coating performance before and after hydrogen charging. Thus, in this section, the simulated groundwater used contained only Na$^+$, Cl$^-$ and SO$_4^{2-}$, as specified in Table 3.

The penetration of hydrogen into the metal can cause lattice distortion within the metal, or generate hydrides. Hydrides were shown to be formed on Ti surfaces under simulated crevice environments (low pH) [48]. Recently, magnesium hydride (MgH$_2$) was reported to be formed during the galvanostatic polarization treatment of Mg ZEK100 alloys, and shown to be responsible for the filiform-like corrosion by acting as a temporary metastable catalyst for hydrogen evolution prior to its decomposition to Mg(OH)$_2$ [49]. Copper hydride (CuH), has been reported to form under reducing conditions, e.g., during copper plating [50–52]. Herein, it is proposed that CuH can be formed during the hydrogen charging process (reaction 13 and 14).

$$H_2O + Cu + e^- \rightarrow CuH_{ads} + OH^- \tag{13}$$

$$CuH_{ads} \rightarrow CuH_{abs} \rightarrow CuH \tag{14}$$

The formation of CuH on the hydrogen-charged Cu sheet and Cu coating surface has been investigated by XRD under an Ar atmosphere at

− 50 °C since CuH is usually unstable [53] and the incident high-energy X-rays would inevitably disturb its presence. As shown in Fig. 5, for several hydrogen-charged samples, the strong diffraction peaks corresponding to the (111), (200), and (220) planes of metallic Cu are observed. In addition, several diffraction peaks with much lower intensities, corresponding to the (002), (200), (103) and (201) faces of CuH [50, 53–55], are also present, with the intensities of these CuH peaks independent of the duration of hydrogen charging. However, the strongest diffraction peak of CuH corresponding to the (101) plane, observed at ~40.7° for hydrides synthesized by conventional chemical methods [50,54], is absent. This probably reflects a grain growth preference of CuH formed on Cu during hydrogen charging.

3.3. The EIS evolution on the hydrogen-free and hydrogen-charged specimens

Fig. 6 shows the EIS spectra recorded on both hydrogen-free and hydrogen-charged samples. For both samples, after 1 h of immersion, the data collected at low frequencies (<10^{-2} Hz) are erratic, despite the corrosion potential of the specimens being stabilized before the EIS measurement. Based on the Kramers–Kronig (K–K) transform [56] results, these erratic data were disregarded. For the hydrogen-free sample, as the immersion time increases from 20 to 44 h, shifts of the low-frequency time constant to lower frequencies and the mid-frequency time constant to higher frequencies are observed, indicating a change in the kinetics of the processes occurring. In addition, the change of the impedance magnitude at the low-frequency limit is minor.

For the hydrogen-charged sample, the EIS spectrum is first collected after 1 h of immersion before hydrogen charging to demonstrate the repeatable coating performance after fabrication by the present method. After 17 days of hydrogen charging, the sample is switched to open circuit, allowing the relaxation of the corrosion potential to a steady-state value (normally within 5 h). Fig. 6d shows two ill-defined responses in the low- to mid-frequency range during immersion. As the immersion time increases from 1 to 20 h, there is a clear decrease in the impedance magnitude at the low-frequency limit, similar to that observed on the hydrogen-free sample. However, as the immersion time increases from 20 to 44 h, the impedance magnitude at the low-frequency limit $|Z|_{f \to 0}$ (f = 0.001 Hz) increases again from 14.7 to 33.5 kΩ·cm^2, indicating a recovery of the coating performance. The hydrogen charging clearly causes different trends in the evolution of the EIS spectra.
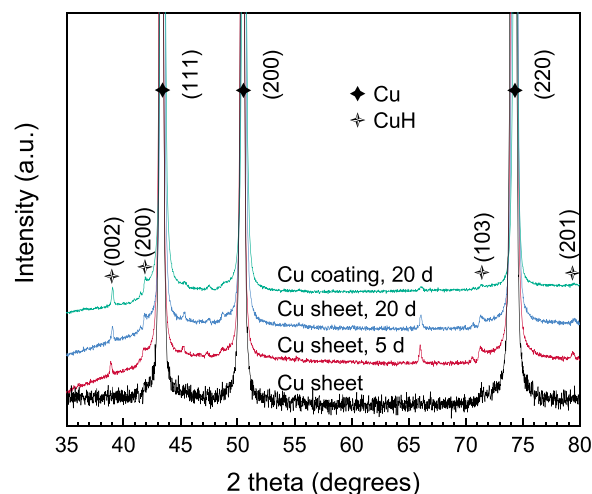

Fig. 5. X-ray diffraction results of the hydrogen-charged Cu sheet and Cu coating surfaces with different duration of hydrogen charging treatment. d, days of hydrogen charging.
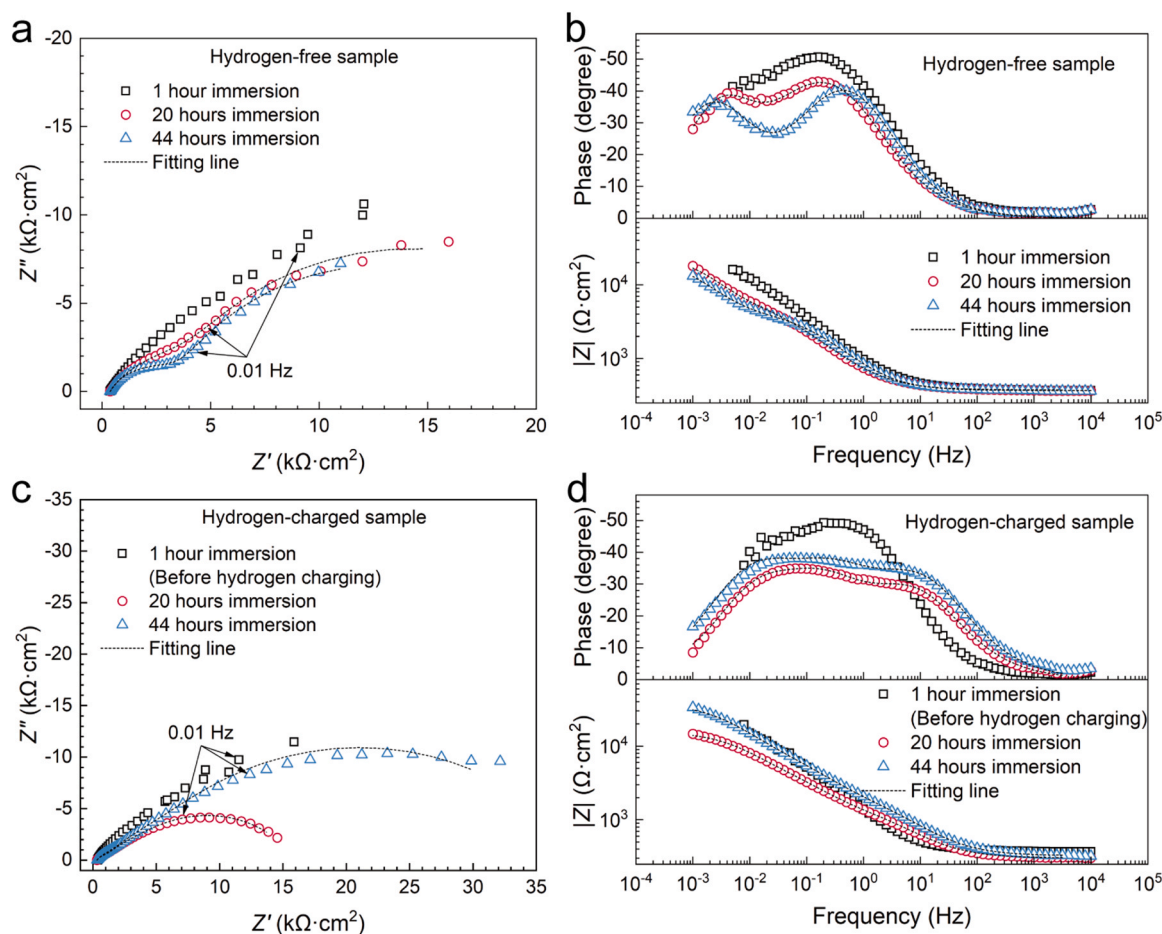
Fig. 6. EIS spectra of the hydrogen-free sample (a, Nyquist plot; b, Bode magnitude and phase angle plot) and hydrogen-charged sample (c, Nyquist plot; d, Bode magnitude and phase angle plot) in simulated groundwater (prepared according to Table 3).

3.4. The surface morphology and chemical composition of the hydrogen-free and hydrogen-charged specimens after immersion

Fig. 7 shows the surface morphologies of the hydrogen-free and hydrogen-charged samples after 44 h of immersion in N$_2$-sparged simulated groundwater. In Fig. 7a, the surface of the hydrogen-free sample is covered with well-crystallized edge-truncated octahedral crystals with 20 facets. The surface layer is quite porous, with observable crevices between crystals. The distribution in crystal size is obtained by measurements on 100 grains in a randomly selected surface area, yielding an average grain size of ∼ 0.4 μm (Fig. 7c). EDX analysis (Fig. 7e, black curve) shows Cu and O are the main elements present with a Cu/O ratio of 2.6. The above results suggest the formation of Cu$_2$O on the surface of the hydrogen-free sample, which is further confirmed by the following XPS analysis.

Fig. 7b shows the rather different surface morphology of the hydrogen-charged sample, with the irregular particles (light color marked as b1 in Fig. 7b) scattered on the sub-layer network formed by thin flakes (dark color marked as b2 in Fig. 7b). The average size of the irregular particles is about 0.23 μm (Fig. 7d), but there is a significant nm-scale substructure. According to the EDX analysis, the hydrogen-charged Cu surface has a similar elemental composition, but with a higher Cu/O ratio of 4.6 (Fig. 7e, red curve), attributable to a larger contribution from Cu. The EDX analysis in Fig. 7f shows that the light-colored particles (marked as b1 in Fig. 7b) have a much higher oxygen content (with a Cu/O ratio of 1.3) than the dark sub-layer (marked as b2 in Fig. 7b).

The chemical constitution on the surface of the hydrogen-free and

hydrogen-charged samples after 44 h of immersion in simulated groundwater was analyzed by XPS. Fig. 8 shows the Cu 2p (a), Cu LMM ((a), inset) and O 1 s (b) spectra of the hydrogen-free sample. To avoid the influence of sample preparation (e.g., that due to the heat generated by cutting the sample with an electric saw) on the surface composition, XPS spectra were recorded after etching the surface to a depth of about 20 nm. However, a weak satellite peak (942–947 eV) was observed suggesting the presence of traces of Cu(II) on the surface. The fitting parameters and results are summarized in Table 5. Since the 2p 3/2 peak (932.49 eV) possibly contains inseparable contributions from Cu(0) and Cu(I) it cannot be used, to determine the Cu(0)/Cu(I) content of the surface unequivocably. To identify the Cu species present, the Cu L$_3$M$_{4,5}$M$_{4,5}$ (LMM) Auger spectrum was fitted as described in reference 57. This analysis confirmed the dominant presence of Cu(I) species on the Cu coating surface [54,57,58].

The O 1 s peak shown in Fig. 8b can be deconvoluted into a peak at 530.38 eV, assigned to oxygen (O$_{lat.}$) in a Cu oxide lattice [54,58], and a broad peak at 532.04 eV with a FWHM of 2.4 eV, which can be assigned to a combination of crystalline H$_2$O (532.1–532.9 eV, [58]), adsorbed hydroxide (–OH) (531.1 eV, [59], 533.2 eV, [60]) and carbonate (533.2 eV, [61], 531.5–532.0 eV, [Avantage software]). Further deconvolution of the 532.04 eV peak is not possible, due to the overlapping of peaks for various possible contributions. The results in Table 5 show the Cu(I)/O$_{lat.}$ Ratio is 2:1, confirming that the oxide formed on the uncharged hydrogen-free Cu coating surface (Fig. 7a) was Cu$_2$O. In oxygen-deficient simulated groundwaters, the formation of Cu$_2$O on the Cu surface has been reported in other studies [11,62].

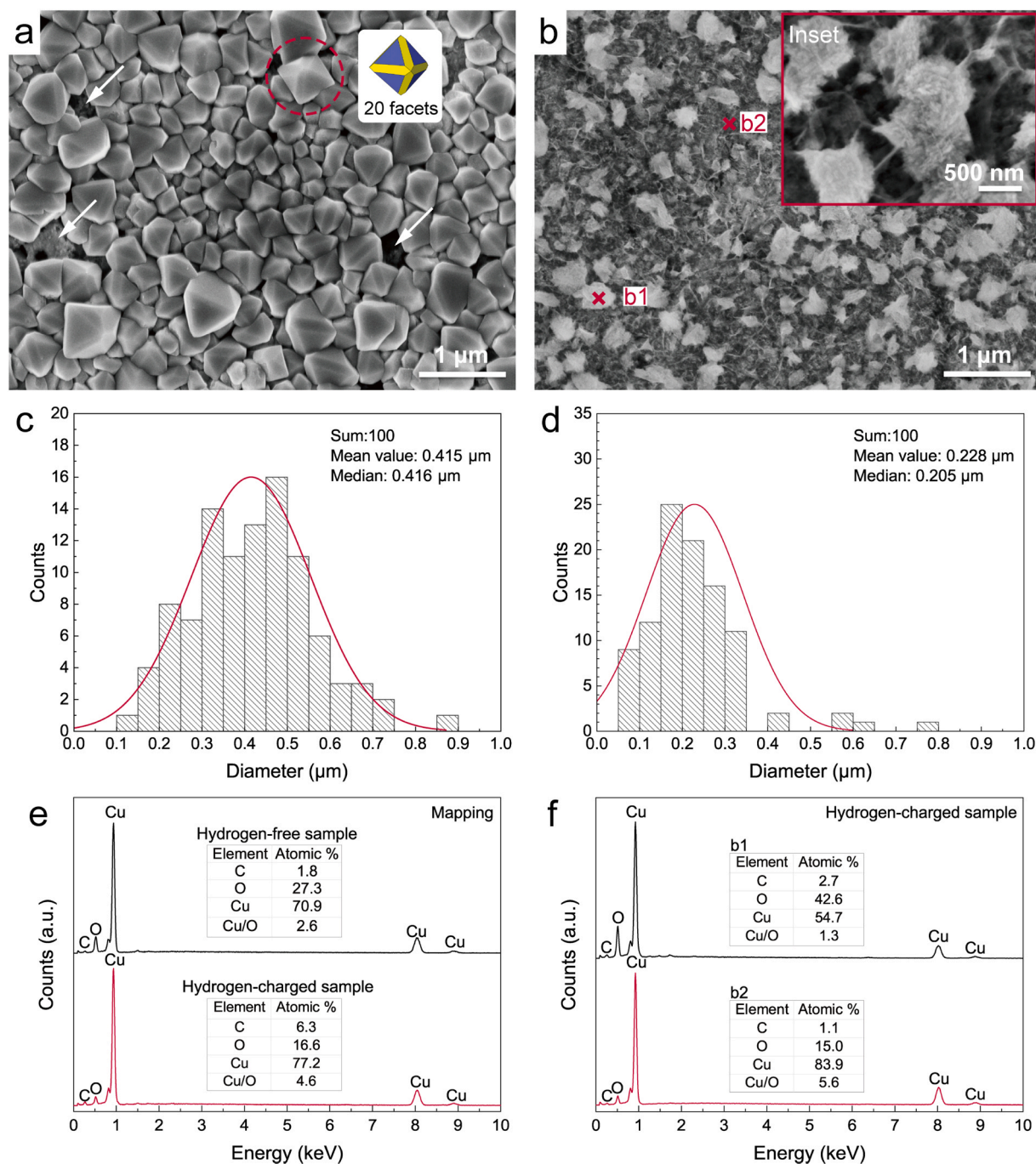Fig. 9 shows a series of XPS depth profiles recorded on the hydrogen-

Fig. 7. SEM images (a, b), histograms of corrosion product particle size distribution as observed in the SEM images (c, d) and EDX spectra (e, f) of the hydrogen-free and hydrogen-charged sample surface after 44 h immersion in N_2-sparged simulated groundwater (prepared according to Table 3).

charged sample after immersion. Fig. 9a shows no satellite peak in the BE region, 942–947 eV, indicating that any Cu(II) species formed during sample preparation were removed by etching. The peak at 932.59–932.64 eV is assigned to Cu(0) or Cu(I) species which cannot be separated. The Cu LMM Auger peak (Fig. 9b) can be deconvoluted into peaks at 918.4 and 916.8 eV, assigned to Cu(0) and Cu(I), respectively [57]. The fitting results show that the relative content of Cu(I) decreases from 89% to 76%, as the etching depth increases from 100 to 220 nm. Fig. 9c shows the deconvolution of the O 1 s peak into two peaks. The peak at 530.03–530.16 eV is assigned to the lattice oxygen in an oxide phase [54,58]. According to the fitting results for the Cu LMM Auger peak (Fig. 9b), when the etching depth is 220 nm, the ratio of Cu(I)/(Cu(I)+Cu(0))= 76.2%. The results in Table 6 show that the total Cu content on

the surface is 20.9 at%. Thus, the Cu(I) content on the surface can be calculated to be,

$$[Cu(I)]_{220\ nm} = 20.9\ at\% \times 76.2\% = 15.9\ at\%.$$

According to Table 6, the lattice oxygen content on the surface is 9.9 at%, and the Cu(I)/$O_{lat.}$ Ratio is therefore 1.6, indicating the existence on the surface of a Cu(I) species with a lower Cu(I)/$O_{lat.}$ Ratio than the stoichiometric Cu_2O.

3.5. The formation of the surface film induced by hydrogen charging

The surface morphology (Fig. 7b), oxygen ratio (Fig. 7e, red curve) and XPS analysis further demonstrate that the surface species on
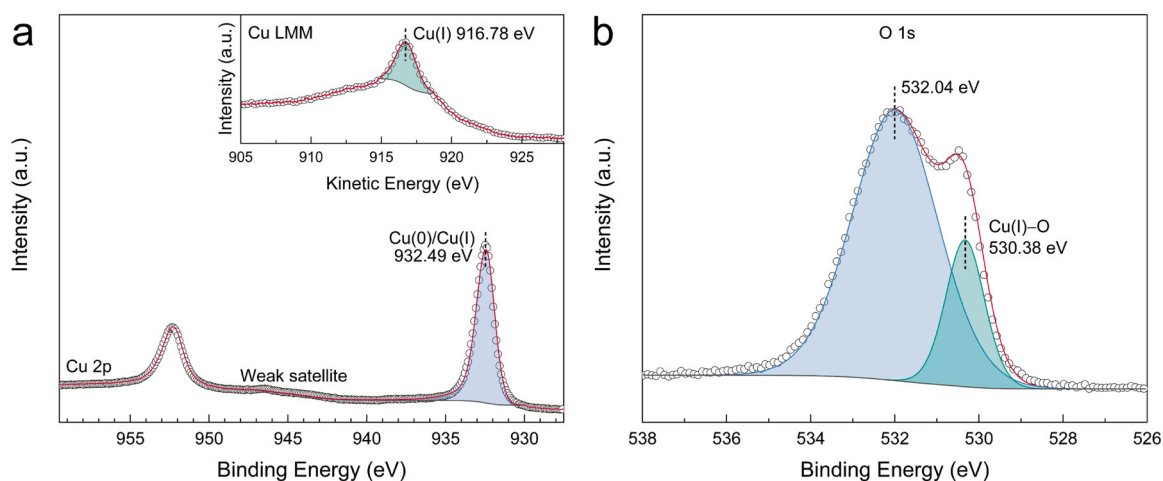
Fig. 8. XPS spectra of Cu 2p (a), Cu LMM (a, inset) and O 1 s (b) obtained from the surface of the hydrogen-free sample etched by 20 nm.

Table 5
XPS results of the hydrogen-free sample surface etched by 20 nm.

	20 nm			Chemical binding, compounds
	BE (eV)	FWHM	at%	
C 1 s	284.80	1.54	33.1	C–(C, H)
	286.70	1.63	4.3	C–OH
	288.98	1.63	2.8	carbonate
O 1 s	530.33	1.09	8.4	Cu(I)–O
	531.99	2.40	34.1	H_2O cryst., –OH, carbonate, et. al
Cu 2p	932.43	1.31	17.3	Cu(I)

hydrogen-charged samples is not only Cu_2O, as observed for the uncharged surface, but a mixture of Cu_2O and other Cu(I) species with low Cu(I)/$O_{lat.}$ Ratios. Under hydrogen charging conditions, the surface would be expected to be cathodically protected, which would restrict the formation of oxide.

In Section 3.2, the formation of CuH on the Cu surface was demonstrated by XRD. As the reducing condition is not maintained during the subsequent immersion period, the highly reactive CuH can decompose into highly reactive Cu particles which oxidize rapidly and sinter to form Cu_2O when exposed to air [51]. Also, CuH decomposition in an alkaline solution containing Cl^- can also lead to the formation of active Cu particles (reactions 15 and 16) [63], which would subsequently be oxidized to Cu_2O (reaction 17). Based on the XPS analyses, the decomposition of CuH could proceed via a CuOH intermediate to Cu_2O (reactions 18 and 19). This would be consistent with the observation of Soroka et. al [54] who demonstrated that CuOH can be formed on the surface of a mixture of CuH and Cu particles stored in water. The observation that the XPS results indicate the existence of another Cu(I) species with lower Cu(I)/$O_{lat.}$ Ratio than Cu_2O indicates the formation of CuOH on the hydrogen-charged sample surface is possible. The XPS fitting results in Table 6 and the calculated ratio between Cu(0)/Cu(I) (based on the Auger spectra (Fig. 9b)), the relative contents of Cu(0), Cu_2O and CuOH as a function of etching depth are summarized in Table 7. It is noted that the content of CuOH gradually increases with the increase in etching depth (Table 7), suggesting that the surface of CuOH is likely converted into Cu_2O (reaction 19) [55].
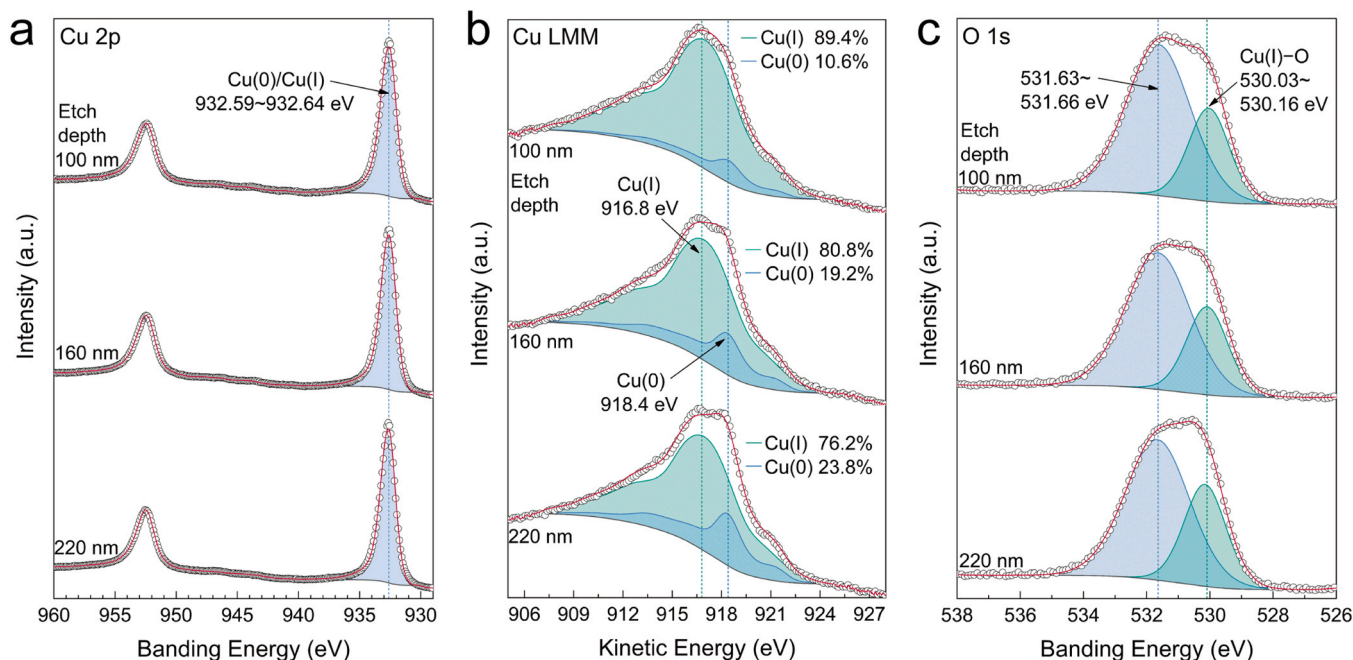

Fig. 9. The depth profiling XPS spectra of Cu 2p (a), Cu LMM (b) and O 1 s (c) obtained from the hydrogen-charged sample surface.
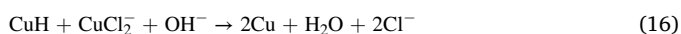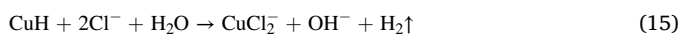
Table 6
The depth profiling XPS results of the hydrogen-charged sample.

	100 nm			160 nm			220 nm			Chemical binding,
	BE (eV)	FWHM	at%	BE (eV)	FWHM	at%	BE (eV)	FWHM	at%	compounds
C 1 s	284.80	1.59	40.7	284.80	1.62	41.7	284.80	1.59	41.8	C–(C, H)
	286.79	1.63	4.3	286.85	1.63	3.6	286.84	1.63	3.9	C–OH
	289.05	1.63	2.7	289.07	1.63	2.6	289.03	1.63	2.6	carbonate
O 1 s	530.03	1.52	9.5	530.09	1.54	9.4	530.16	1.57	9.9	Cu(I)–O
	531.63	2.40	24.5	531.63	2.40	22.9	531.66	2.40	20.9	H_2O cryst., –OH, carbonate, et. al
Cu 2p	932.59	1.55	18.3	932.60	1.50	19.8	932.64	1.47	20.9	Cu(0), Cu(I)

Table 7
Ratio of Cu(0), CuOH and Cu_2O on the surface of the hydrogen-charged sample.

Etch depth (nm)	Cu (0) (%)	CuOH (%)	Cu_2O (%)	$CuOH/Cu_2O$
100	16.9	23.1	60.0	0.38
160	28.8	21.2	50.0	0.42
220	33.4	26.1	40.5	0.64

$$CuH + 2Cl^- + H_2O \rightarrow CuCl_2^- + OH^- + H_2\uparrow \tag{15}$$

$$CuH + CuCl_2^- + OH^- \rightarrow 2Cu + H_2O + 2Cl^- \tag{16}$$

$$4Cu + O_2 \rightarrow 2Cu_2O \tag{17}$$

$$CuH + H_2O \rightarrow CuOH + H_2\uparrow \tag{18}$$

$$2CuOH \rightarrow Cu_2O + H_2O \tag{19}$$

Since the XRD analysis (Fig. 5) shows no diffraction peaks for CuOH and Cu_2O on the hydrogen-charged sample, it is clear that CuOH and Cu_2O are formed during the immersion period after hydrogen charging.

3.6. The cross-sectional morphology and chemical constitution of the hydrogen-charged specimen

The cross-sectional morphology and chemical composition of the hydrogen-charged sample are shown in Fig. 10. Fig. 10a shows a very uniform Cu coating on the carbon steel substrate after hydrogen charging for 17 days followed by 44 h of immersion. The SEM image and the corresponding EDX map for the entire coating, Fig. 10b and c, show no observable coating delamination or damage with the orderly distribution of Cu, Ni and Fe elements remaining undisturbed despite the extensive charging period and subsequent exposure. The fact that no blisters appear in the Cu layer after charging shows that H_{abs} recombination at defects in the Cu layer is negligible under the current charging conditions, compared to hydrogen molecule desorption losses at the Cu surface (reaction 2 and 3). The formation of Cu_2O, CuOH cannot be detected on the scale of the images in Fig. 10c and also due to the strong O signal from the resin. At the greater magnification achieved in the FIB/SEM images (Fig. 10d-f) the film is shown to be porous with a distribution of irregular particles on top, consistent with the analysis in Fig. 7b.

3.7. EIS fitting

The SEM image in Fig. 7a shows the film formed on the surface of the hydrogen-free sample is porous. Thus, an equivalent circuit with two time constants, Fig. 11a, is appropriate to fit the spectra shown in Fig. 6. Such a circuit has been used commonly to describe the corroded surface on Cu [64–68]. In the equivalent circuit in Fig. 11a, constant phase elements (CPE), calculated according to Eq. (20), were used to represent non-ideal capacitances, where Y_0 represents the admittance modulus ($s^n \cdot \Omega^{-1} \cdot cm^{-2}$), ω the angular frequency, and n is a constant with a value between 0 and 1. The surface inhomogeneities and the porous structure of the corrosion film formed on the Cu surface (in Fig. 7) would result in

frequency dispersion [12,69], leading to the deviation of the n value from 1. In this circuit (Fig. 11a), R_s represents the solution resistance, Q_f is a constant phase element (CPE) representing the film capacitance, R_f is the film resistance, Q_{dl} and R_{ct} represent the double-layer capacitance and charge transfer resistance at the Cu/solution interface. Considering the alkaline condition produced by hydrogen charging, a layer of adsorbed OH^- is probably formed on the hydrogen-charged surface [70]. Thus, the EIS data of the hydrogen-charged sample are fitted using the equivalent circuit with three time constants, as shown in Fig. 11b. In this circuit, Q_{ads} and R_{ads} represent the capacitance and resistance of the adsorbed layer. Since the EIS data collected after 1 h of immersion was erratic at low frequencies (<0.01 Hz) for both uncharged and charged samples, only the data recorded after 20 and 44 h of immersion were fitted, with the fitting parameters listed in Table 8.

$$Q = 1/[Y_0(j\omega)^n] \tag{20}$$

For the hydrogen-free sample, the film resistance (R_f) decreases with immersion time suggesting an increase in film porosity in the presence of chloride ions. Since only a slight increase in the charge transfer resistance (R_{ct}) is observed, this Faradaic resistance increase may be partially compensated by an increase in film thickness.

For the hydrogen-charged sample, the resistance of the adsorbed layer (R_{ads}) increases with immersion time, indicating that the adsorption of OH^- continues during immersion. In addition, both R_f and R_{ct} increase with immersion time, suggesting an improved corrosion resistance of the Cu surface. This is correlated with the formation of a CuOH/Cu_2O film caused by CuH decomposition (reactions 18 and 19). It is consistent with the surface and cross-sectional observations, EDS analyses and XPS analyses in Figs. 7, 9 and 10. The low values of n were to be expected given the rough and porous nature of the surface films (Fig. 7a and b) and the variation in composition with the thickness of the film on the hydrogen charged surface indicated by the XPS spectra.

4. Summary and conclusions

1) The susceptibility of a Cu coating on carbon steel to hydrogen permeation in simulated Chinese groundwater (Beishan area) has been investigated under hydrogen charging conditions. The steady-state hydrogen permeation current through carbon steel (Q235) was found to be significantly decreased by a Cu coating with a thickness of several micrometers.

2) The average diffusion coefficient measured on the Cu-coated steel was two orders of magnitude lower than on the uncoated steel, and decreased as the Cu layer thickness was increased. The calculated effective diffusion coefficient of carbon steel with a 10 μm Cu coating (1.5×10^{-9} $cm^2 \cdot s^{-1}$) was similar to the reported diffusion coefficient for pure Cu (1.8×10^{-9} $cm^2 \cdot s^{-1}$).

3) Detailed microanalytical analysis (including EDS, XPS and XRD) indicates that copper hydride (CuH) was formed during the hydrogen charging process with its subsequent decomposition leading to the formation of a partially protective layer composed of CuOH and Cu_2O when exposed to simulated groundwater for 44 h.
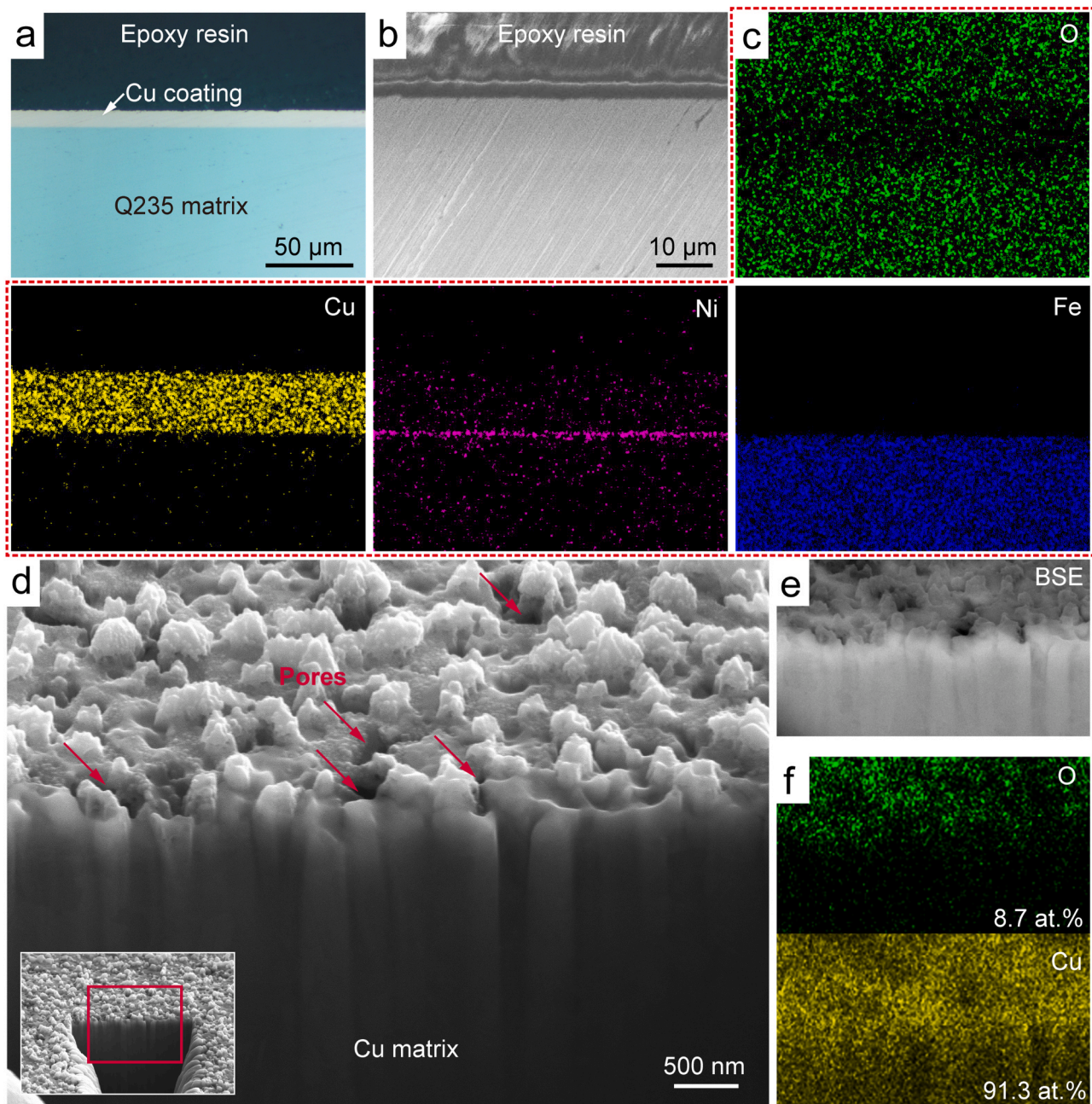
Fig. 10. Cross section morphologies (a, b, d and e) and elemental analysis (c and f) of the Q235 specimen with a ~600 nm Ni layer and 10 μm Cu coating after 17 days of hydrogen charging. a, the metallographic image of the cross section; b and c, the SEM image and the corresponding EDX mapping of the cross section; d, e and f, FIB-SEM images and the corresponding EDX analysis of the cross section.
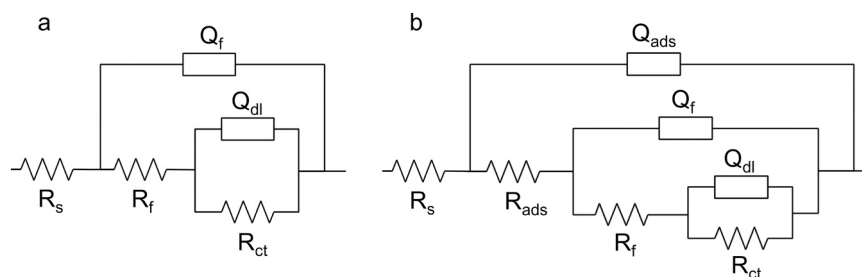

Fig. 11. Equivalent circuits used for fitting the EIS spectra recorded on the hydrogen-free (a) and hydrogen-charged (b) specimens. R_s represents the solution resistance; Q_{ads} is a constant phase element (CPE) representing the capacitance of the adsorbed layer; R_{ads} represents the resistance of the adsorbed layer; Q_f and R_f are the film capacitance and resistance; Q_{dl} and R_{ct} represent the double-layer capacitance and charge transfer resistance at the Cu/solution interface.

Table 8
Fitting results of EIS data in simulated groundwater.

	Immersion time (hour)	R_s ($\Omega \cdot cm^2$)	$Y_{0\text{-ads}}$ ($s^n \cdot \Omega^{-1} \cdot cm^{-2}$)	n_{ads}	R_{ads} ($\Omega \cdot cm^2$)	$Y_{0\text{-f}}$ ($s^n \cdot \Omega^{-1} \cdot cm^{-2}$)	n_f	R_f ($\Omega \cdot cm^2$)	$Y_{0\text{-dl}}$ ($s^n \cdot \Omega^{-1} \cdot cm^{-2}$)	n_{dl}	R_{ct} ($\Omega \cdot cm^2$)
Hydrogen-free Sample	20	373.1	—	—	—	5.525×10^{-4}	0.70	6994	2.629×10^{-3}	0.86	18260
	44	367.2	—	—	—	3.932×10^{-4}	0.74	4023	3.786×10^{-3}	0.81	18632
Hydrogen-Charged Sample	20	302.5	1.19×10^{-4}	0.70	1374	3.44×10^{-4}	0.70	6227	9.34×10^{-4}	0.77	7936
	44	324.7	7.79×10^{-5}	0.70	2161	1.68×10^{-4}	0.70	9915	3.71×10^{-4}	0.74	26050

4) No damage to the Cu coating-steel interface was observed after 17 days of hydrogen charging (with a charging current of -500 $\mu A \cdot cm^{-2}$).

Although the hydrogen charging conditions in this work were considerably more aggressive than those sustainable under nuclear waste disposal conditions, no significant damage was observed at the Cu coating/steel interface as a consequence of hydrogen permeation under the current electrochemical hydrogen charging conditions. Therefore, the lower hydrogen penetration under disposal conditions should result in even less damage. However, since Cu corrosion is expected to be driven by reaction with sulphide in the groundwater, experiments in sulphide-containing solutions are on-going.

CRediT authorship contribution statement

Xiangju Liu: Methodology, Investigation, Resources, Formal analysis, Writing – original draft. **Nazhen Liu:** Conceptualization, Formal analysis, Writing – review & editing, Project administration, Funding acquisition. **James J. Noël:** Conceptualization, Writing – review & editing. **David W. Shoesmith:** Writing – review & editing. **Jian Chen:** Writing – review & editing. **Baorong Hou:** Supervision, Funding acquisition.

Declaration of Competing Interest

The authors declare that they have no known competing financial interests or personal relationships that could have appeared to influence the work reported in this paper.

Data Availability

The authors do not have permission to share data.

Acknowledgements

References

[1] J. Chen, M. Behazin, J. Binns, K. Birch, A. Blyth, S. Briggs, J. Freire-Canosa, G. Cheema, R. Crowe, D. Doyle, F. Garisto, J. Giallonardo, M. Gobien, R. Guo, S. Hirschorn, M. Hobbs, M. Ion, J. Jacyk, H. Kasani, P. Keech, E. Kremer, C. Lawrence, H. Leung, K. Liberda, T. Liyanage, J. McKelvie, C. Medri, M. Mielcarek, L. Kennell-Morrison, A. Murchison, A. Parmenter, M.S.-R. Castejon, U. Stahmer, Y. Sui, E. Sykes, M. Sykes, T. Yang, X. Zhang, B. Zhao, Technical program for long-term management of Canada's used nuclear fuel – annual report 2018, NWMO-TR-2019-01, Nuclear Waste Management Organization, Toronto, 2019.

[2] N. Liu, L. Wu, Z. Qin, D.W. Shoesmith, Roles of radiolytic and externally generated H_2 in the corrosion of fractured spent nuclear fuel, Environ. Sci. Technol. 50 (22) (2016) 12348–12355, https://doi.org/10.1021/acs.est.6b04167.

[3] Z. Pan, Q. Qian, Strategy study for high-level radioactive waste disposal, Atomic Energy Press, Beijing, 2009 (in Chinese).

[4] D.W. Shoesmith, Assessing the corrosion performance of high-level nuclear waste containers, Corrosion 62 (8) (2006) 703–722, https://doi.org/10.5006/1.3278296.

[5] D.S. Hall, M. Behazin, W. Jeffrey Binns, P.G. Keech, An evaluation of corrosion processes affecting copper-coated nuclear waste containers in a deep geological repository, Prog. Mater. Sci. 118 (2020), 100766, https://doi.org/10.1016/j.pmatsci.2020.100766.

[6] F. King. Corrosion of carbon steel under anaerobic conditions in a repository for SF and HLW in opalinus clay, Technical Report 08–12. nagra. Wettingen, Switzerland. 2008.

[7] F. King, D.W. Shoesmith, Nuclear waste canister materials: corrosion behaviour and long-term performance in geological repository systems, in: J. Ahn, M. Apted (Eds.), Geological repository systems for safe disposal of spent nuclear fuels and radioactive waste, Chapter 13, Woodhead Publishing Limited, Cambridge, UK, 2010, pp. 379–420.

[8] M. Wu, M. Behazin, J. Nam, P. Keech, Internal corrosion of used fuel container, NWMO-TR-2019-02, Nuclear Waste Management Organization, Toronto, 2019.

[9] T. Martino, R. Partovi-Nia, J. Chen, Z. Qin, D.W. Shoesmith, Mechanisms of film growth on copper in aqueous solutions containing sulphide and chloride under voltammetric conditions, Electro Acta 127 (2014) 439–447, https://doi.org/10.1016/j.electacta.2014.02.050.

[10] M. Guo, J. Chen, T. Martino, C. Lilja, J.A. Johansson, M. Behazin, W.J. Binns, P.G. Keech, J.J. Noël, D.W. Shoesmith, The nature of the copper sulfide film grown on copper in aqueous sulfide and chloride solutions, Mater. Corros. 72 (1–2) (2021) 300–307, https://doi.org/10.1002/maco.202011710.

[11] T. Kosec, Z. Qin, J. Chen, A. Legat, D.W. Shoesmith, Copper corrosion in bentonite/saline groundwater solution: effects of solution and bentonite chemistry, Corros. Sci. 90 (2015) 248–258, https://doi.org/10.1016/j.corsci.2014.10.017.

[12] J. Chen, Z. Qin, D.W. Shoesmith, Long-term corrosion of copper in a dilute anaerobic sulfide solution, Electro Acta 56 (23) (2011) 7854–7861, https://doi.org/10.1016/j.electacta.2011.04.086.

[13] J. Chen, Z. Qin, T. Martino, D.W. Shoesmith, Non-uniform film growth and micro/macro-galvanic corrosion of copper in aqueous sulphide solutions containing chloride, Corros. Sci. 114 (2017) 72–78, https://doi.org/10.1016/j.corsci.2016.10.024.

[14] J. Chen, Z. Qin, L. Wu, J.J. Noël, D.W. Shoesmith, The influence of sulphide transport on the growth and properties of copper sulphide films on copper, Corros. Sci. 87 (2014) 233–238, https://doi.org/10.1016/j.corsci.2014.06.027.

[15] X. He, T. Ahn, J.-P. Gwo, Corrosion of copper as a nuclear waste container material in simulated anoxic granitic groundwater, Corrosion 74 (2) (2017) 158–168, https://doi.org/10.5006/2471.

[16] S. Kaufhold, R. Dohrmann, J. Gröger-Trampe, Reaction of native copper in contact with pyrite and bentonite in anaerobic water at elevated temperature, Corros. Eng. Sci. Technol. 52 (5) (2017) 349–358, https://doi.org/10.1080/1478422X.2017.1292201.

[17] B. Reddy, C. Padovani, N.R. Smart, A.P. Rance, A. Cook, A. Milodowski, L. Field, S. Kemp, N. Diomidis, Further results on the in situ anaerobic corrosion of carbon steel and copper in compacted bentonite exposed to natural Opalinus Clay porewater containing native microbial populations, Mater. Corros. 72 (1–2) (2020) 268–281, https://doi.org/10.1002/maco.202011785.

[18] J.-M. Chen, J.-K. Wu, Hydrogen diffusion through copper-plated AISI 4140 steels, Corros. Sci. 33 (5) (1992) 657–666, https://doi.org/10.1016/0010-938X(92)90100-H.

[19] T.E. Standish, L.J. Braithwaite, D.W. Shoesmith, J.J. Noël, Influence of area ratio and chloride concentration on the galvanic coupling of copper and carbon steel, J. Electrochem Soc. 166 (11) (2019) C3448–C3455, https://doi.org/10.1149/2.0521911jes.

[20] T.E. Standish, J. Chen, R. Jacklin, P. Jakupi, S. Ramamurthy, D. Zagidulin, P.G. Keech, D.W. Shoesmith, Corrosion of copper-coated steel high level nuclear waste containers under permanent disposal conditions, Electro Acta 211 (2016) 331–342, https://doi.org/10.1016/j.electacta.2016.05.135.

[21] T.E. Standish, D. Zagidulin, S. Ramamurthy, P.G. Keech, J.J. Noël, D.W. Shoesmith, Galvanic corrosion of copper-coated carbon steel for used nuclear fuel containers, Corros. Eng. Sci. Technol. 52 (sup1) (2017) 65–69, https://doi.org/10.1080/1478422X.2017.1306972.

[22] Y.-S. Chen, H. Lu, J. Liang, A. Rosenthal, H. Liu, G. Sneddon, I. McCarroll, Z. Zhao, W. Li, A. Guo, J.M. Cairney, Observation of hydrogen trapping at dislocations, grain boundaries, and precipitates, Science 367 (6474) (2020) 171–175, https://doi.org/10.1126/science.aaz0122.

[23] S.K. Dwivedi, M. Vishwakarma, Hydrogen embrittlement in different materials: a review, Int J. Hydrog. Energ. 43 (46) (2018) 21603–21616, https://doi.org/10.1016/j.ijhydene.2018.09.201.

[24] E. Ohaeri, U. Eduok, J. Szpunar, Hydrogen related degradation in pipeline steel: a review, Int J. Hydrog. Energ. 43 (31) (2018) 14584–14617, https://doi.org/10.1016/j.ijhydene.2018.06.064.

[25] N. Saini, C. Pandey, M.M. Mahapatra, Effect of diffusible hydrogen content on embrittlement of P92 steel, Int J. Hydrog. Energ. 42 (27) (2017) 17328–17338, https://doi.org/10.1016/j.ijhydene.2017.05.214.

[26] Y.H. Fan, B. Zhang, J.Q. Wang, E.-H. Han, W. Ke, Effect of grain refinement on the hydrogen embrittlement of 304 austenitic stainless steel, J. Mater. Sci. Technol. 35 (10) (2019) 2213–2219, https://doi.org/10.1016/j.jmst.2019.03.043.

[27] Y. Qiao, D. Xu, S. Wang, Y. Ma, J. Chen, Y. Wang, H. Zhou, Effect of hydrogen charging on microstructural evolution and corrosion behavior of Ti-4Al-[2]V–[1]Mo-1Fe alloy, J. Mater. Sci. Technol. 60 (2021) 168–176, https://doi.org/10.1016/j.jmst.2020.06.010.

[28] M.A.V. Devanathan, Z. Stachurski, The mechanism of hydrogen evolution on iron in acid solutions by determination of permeation rates, J. Electrochem Soc. 111 (5) (1964) 619–623, https://doi.org/10.1149/1.2426195.

[29] Y. Huang, Corrosion failure of marine steel in sea-mud containing sulfate reducing bacteria, Mater. Corros. 55 (2) (2004) 124–127, https://doi.org/10.1002/maco.200303698.

[30] M. Zheng, Q. Zhang, Y. Huang, D. Lu, X. Yu, Y. Liu, Determination of representative ground-water for corrosion assessment of candidate materials used in beishan area preselected for high-level radioactive waste disposal repository, J. Chin. Soc. Corros. Prot. 36 (2) (2016) 185–190.

[31] L. Zhang, H.-j Shen, J.-y Sun, Y.-n Sun, Y.-C. Fang, W.-h Cao, Y.-y Xing, M.-x Lu, Effect of calcareous deposits on hydrogen permeation in X80 steel under cathodic protection, Mater. Chem. Phys. 207 (2018) 123–129, https://doi.org/10.1016/j.matchemphys.2017.12.015.

[32] X. Liu, Y. Huang, J. Li, D. Yang, Y. Xu, H.-J. Kunte, Effect of microbial hydrogen consumption on the hydrogen permeation behaviour of AISI 4135 steel under cathodic protection, Int J. Hydrog. Energ. 45 (7) (2020) 4054–4064, https://doi.org/10.1016/j.ijhydene.2019.12.058.

[33] L. Simoni, J.Q. Caselani, L.B. Ramos, R.M. Schroeder, C. de Fraga Malfatti, The influence of calcareous deposits on hydrogen uptake and embrittlement of API 5CT P110 steel, Corros. Sci. 118 (2017) 178–189, https://doi.org/10.1016/j.corsci.2017.02.007.

[34] C. Li, M. Du, J. Qiu, J. Zhang, C. Gao, Influence of temperature on the protectiveness and morphological characteristics of calcareous deposits polarized by Galvanostatic mode, Acta Metall. Sin. -Engl. Lett. 27 (1) (2014) 131–139, https://doi.org/10.1007/s40195-013-0010-6.

[35] W. Sun, G. Liu, L. Wang, Y. Li, A mathematical model for modeling the formation of calcareous deposits on cathodically protected steel in seawater, Electro Acta 78 (2012) 597–608, https://doi.org/10.1016/j.electacta.2012.06.056.

[36] S. Yoshizawa, T. Tsuruta, K. Yamakawa, Development of nickel plating method in electrochemical measurement of hydrogen content in steel, Zair. -to-kankyo 24 (1975) 511–515, https://doi.org/10.3323/jcorr1974.24.10_511.

[37] Y. Huang, X. Liu, Q. Zhang, Y. Xu, H.-J. Kunte, R. De Marco, Hydrogen release from carbon steel in chloride solution under anodic polarization, Int J. Hydrog. Energ. 45 (4) (2020) 3307–3315, https://doi.org/10.1016/j.ijhydene.2019.11.218.

[38] A. Lasia, D. Grégoire, General model of electrochemical hydrogen absorption into metals, J. Electrochem Soc. 142 (10) (1995) 3393, https://doi.org/10.1149/1.2050267.

[39] T. Zhang, W. Zhao, T. Li, Y. Zhao, Q. Deng, Y. Wang, W. Jiang, Comparison of hydrogen embrittlement susceptibility of three cathodic protected subsea pipeline steels from a point of view of hydrogen permeation, Corros. Sci. 131 (2018) 104–115, https://doi.org/10.1016/j.corsci.2017.11.013.

[40] M. Moshref-javadi, H. Edris, A. Shafyei, H. Salimi-Jazi, Diffusion behavior of hydrogen through thermally sprayed coating of 316L stainless steel, Int J. Hydrog. Energy 42 (9) (2017) 6409–6419, https://doi.org/10.1016/j.ijhydene.2016.11.026.

[41] E. Owczarek, T. Zakroczymski, Hydrogen transport in a duplex stainless steel, Acta Mater. 48 (12) (2000) 3059–3070, https://doi.org/10.1016/S1359-6454(00)00122-1.

[42] Q. Liu, Q. Zhou, J. Venezuela, M. Zhang, J. Wang, A. Atrens, A review of the influence of hydrogen on the mechanical properties of DP, TRIP, and TWIP advanced high-strength steels for auto construction, Corros. Rev. 34 (3) (2016) 127–152, https://doi.org/10.1515/corrrev-2015-0083.

[43] M.A.V. Devanathan, Z. Stachurski, The adsorption and diffusion of electrolytic hydrogen in palladium, Proc. R. Soc. Lond. 270 (1340) (1962) 90–102, https://doi.org/10.1098/rspa.1962.0205.

[44] E. Fallahmohammadi, F. Bolzoni, G. Fumagalli, G. Re, G. Benassi, L. Lazzari, Hydrogen diffusion into three metallurgical microstructures of a C–Mn X65 and low alloy F22 sour service steel pipelines, Int. J. Hydrog. Energy 39 (25) (2014) 13300–13313, https://doi.org/10.1016/j.ijhydene.2014.06.122.

[45] K.C. Ou, J.K. Wu, Effect of calcareous deposits formation on the hydrogen absorption of steel, Mater. Chem. Phys. 48 (1) (1997) 52–55, https://doi.org/10.1016/S0254-0584(97)80076-4.

[46] W. Smith, S. Paul, Natural deposit coatings on steel during cathodic protection and hydrogen ingress, Coatings 5 (4) (2015) 816–829, https://doi.org/10.3390/coatings5040816.

[47] W. Chu, L. Qiao, J. Li, Y. Su, Y. Yan, Y. Bai, X. Ren, H. Huang, Hydrogen embrittlement and stress corrosion cracking, Science Press, Beijing, 2013.

[48] L. Yan, S. Ramamurthy, J.J. Noël, D.W. Shoesmith, Hydrogen absorption into alpha titanium in acidic solutions, Electro Acta 52 (3) (2006) 1169–1181, https://doi.org/10.1016/j.electacta.2006.07.017.

[49] W. Jeffrey Binns, F. Zargarzadah, V. Dehnavi, J. Chen, J.J. Noël, D.W. Shoesmith, Physical and electrochemical evidence for the role of a Mg hydride species in Mg alloy corrosion, Corrosion 75 (1) (2018) 58–68, https://doi.org/10.5006/2918.

[50] N.P. Fitzsimons, W. Jones, P.J. Herley, Studies of copper hydride. Part 1.—synthesis and solid-state stability, J. Chem. Soc., Faraday Trans. 91 (4) (1995) 713–718, https://doi.org/10.1039/FT9959100713.

[51] E. Bennett, T. Wilson, P.J. Murphy, K. Refson, A.C. Hannon, S. Imberti, S.K. Callear, G.A. Chass, S.F. Parker, How the surface structure determines the properties of CuH, Inorg. Chem. 54 (5) (2015) 2213–2220, https://doi.org/10.1021/ic5027009.

[52] D. Yin, H.A. Murdoch, B.C. Hornbuckle, E. Hernandez-Rivera, M.K. Dunstan, Investigation of anomalous copper hydride phase during magnetic field-assisted electrodeposition of copper, Electrochem Commun. 98 (2019) 96–100, https://doi.org/10.1016/j.elecom.2018.11.018.

[53] R. Burtovyy, D. Włosewicz, A. Czopnik, M. Tkacz, Heat capacity of copper hydride, Thermochim. Acta 400 (1) (2003) 121–129, https://doi.org/10.1016/S0040-6031(02)00489-6.

[54] I.L. Soroka, A. Shchukarev, M. Jonsson, N.V. Tarakina, P.A. Korzhavyi, Cuprous hydroxide in a solid form: does it exist? Dalton Trans. 42 (26) (2013) 9585–9594, https://doi.org/10.1039/C3DT50351H.

[55] P.A. Korzhavyi, I.L. Soroka, E.I. Isaev, C. Lilja, B. Johansson, Exploring monovalent copper compounds with oxygen and hydrogen, Proc. Natl. Acad. Sci. USA 109 (3) (2012) 686–689, https://doi.org/10.1073/pnas.1115834109.

[56] E. Barsoukov, J.R. Macdonald. Impedance Spectroscopy: Theory, Experiment, and Applications, second ed., John Wiley & Sons, Inc,, 2005, p. 149.

[57] M.C. Biesinger, Advanced analysis of copper X-ray photoelectron spectra, Surf. Interface Anal. 49 (13) (2017) 1325–1334, https://doi.org/10.1002/sia.6239.

[58] L. Trotochaud, A.R. Head, S. Pletincx, O. Karslıoğlu, Y. Yu, A. Waldner, L. Kyhl, T. Hauffman, H. Terryn, B. Eichhorn, H. Bluhm, Water adsorption and dissociation on polycrystalline copper oxides: effects of environmental contamination and experimental protocol, J. Phys. Chem. B 122 (2) (2018) 1000–1008, https://doi.org/10.1021/acs.jpcb.7b10732.

[59] X. Deng, T. Herranz, C. Weis, H. Bluhm, M. Salmeron, Adsorption of water on Cu_2O and Al_2O_3 thin Films, J. Phys. Chem. C. 112 (26) (2008) 9668–9672, https://doi.org/10.1021/jp800494r.

[60] H.B. Yao, Y. Li, A.T.S. Wee, An XPS investigation of the oxidation/corrosion of melt-spun Mg, Appl. Surf. Sci. 158 (1) (2000) 112–119, https://doi.org/10.1016/S0169-4332(99)00593-0.

[61] M. Santamaria, F. Di Quarto, S. Zanna, P. Marcus, Initial surface film on magnesium metal: a characterization by X-ray photoelectron spectroscopy (XPS) and photocurrent spectroscopy (PCS), Electro Acta 53 (3) (2007) 1314–1324, https://doi.org/10.1016/j.electacta.2007.03.019.

[62] I. Betova, M. Bojinov, C. Lilja, Hydrogen generation during interaction of oxide covered copper with deoxygenated aqueous solution, Electro Acta 274 (2018) 143–151, https://doi.org/10.1016/j.electacta.2018.04.057.

[63] J.C. Warf, The decomposition kinetics of copper hydride in the presence of electrolytes, J. Inorg. Nucl. Chem. 19 (3) (1961) 304–313, https://doi.org/10.1016/0022-1902(61)80120-6.

[64] R.K. Singh Raman, P. Chakraborty Banerjee, D.E. Lobo, H. Gullapalli, M. Sumandasa, A. Kumar, L. Choudhary, R. Tkacz, P.M. Ajayan, M. Majumder, Protecting copper from electrochemical degradation by graphene coating, Carbon 50 (11) (2012) 4040–4045, https://doi.org/10.1016/j.carbon.2012.04.048.

[65] E. Huttunen-Saarivirta, P. Rajala, M. Bomberg, L. Carpen, Laboratory study of interactions between copper and microorganisms in oxic groundwater (English), Environ. Geotech. 7 (2) (2020) 110–120, https://doi.org/10.1680/jenge.17.00077.

[66] K.R. Chasse, A.J. Scardino, G.W. Swain, Corrosion and fouling study of copper-based antifouling coatings on 5083 aluminum alloy, Prog. Org. Coat. 141 (2020), 105555, https://doi.org/10.1016/j.porgcoat.2020.105555.

[67] S. Chen, D. Zhang, Study of corrosion behavior of copper in 3.5 wt% NaCl solution containing extracellular polymeric substances of an aerotolerant sulphate-reducing bacteria, Corros. Sci. 136 (2018) 275–284, https://doi.org/10.1016/j.corsci.2018.03.017.

[68] P. Yi, C. Dong, K. Xiao, C. Man, X. Li, In-situ investigation of the semiconductive properties and protective role of Cu_2O layer formed on copper in a borate buffer solution, J. Electro Chem. 809 (2018) 52–58, https://doi.org/10.1016/j.jelechem.2017.12.028.

[69] J. Chen, Z. Qin, D.W. Shoesmith, Kinetics of corrosion film growth on copper in neutral chloride solutions containing small concentrations of sulfide, J. Electrochem Soc. 157 (10) (2010) C338, https://doi.org/10.1149/1.3478570.

[70] G. Niaura, Surface-enhanced Raman spectroscopic observation of two kinds of adsorbed OH$^-$ ions at copper electrode, Electro Acta 45 (21) (2000) 3507–3519, https://doi.org/10.1016/S0013-4686(00)00434-5.